Avrupa Bilim ve Teknoloji Dergisi
Sayı 21, S. 285-300, Ocak 2021

Araştırma Makalesi

www.ejosat.com ISSN:2148-2683

European Journal of Science and Technology
No. 21, pp. 285-300, January 2021

Research Article

Crust and Uppermost Mantle Velocity Structure beneath the East Anatolian Fault Zone from Joint Inversion of P-Receiver Functions and Rayleigh Wave Group Velocities

Hamdi Alkan[1*]

[1*] Van Yüzüncü Yıl University, Faculty of Engineering, Departmant of Geophysics, Van, Turkey, (ORCID: 0000-0003-3912-7503), hamdialkan@yyu.edu.tr

(First received 30 Ekim 2020 and in final form 18 Ocak 2021)

(**DOI:** 10.31590/ejosat.818592)

ATIF/REFERENCE: Alkan, H. (2021). Crust and Uppermost Mantle Velocity Structure beneath the East Anatolian Fault Zone from Joint Inversion of P-Receiver Functions and Rayleigh Wave Group Velocities. *European Journal of Science and Technology*, (21), 285-300.

Abstract

The East Anatolian Fault Zone (EAFZ) is an active plate boundary where an intense earthquake activity has occurred from past to present. This activity is highly related to the geodynamic structure of the region. Because of the northward motion of Arabian plate and southward motion of the Eurasian plate, the Anatolian plate has attempted to escape westward with anticlockwise rotation. This tectonic movement cause the development of important tectonic structures. In relation to these active plate motions, the S-wave velocity structure of the EAFZ intersecting the North Anatolian Fault Zone (NAFZ) in the northeast and the Dead Sea Fault Zone (DSFZ) in the southwest is very important in interpretation the tectonic structure of the region. In this study, it was applied on the joint inversion technique of P-wave receiver functions and Rayleigh wave group velocities by using the data collected from eight broadband stations along the EAFZ. The P-receiver functions were obtained by using approximately eighty teleseismic events seperately for each station, recorded by the three-component broadband seismometers. On the other hand, for the Rayleigh wave group velocity dispersion curves, twenty-one local earthquakes which have focal depth less than 50 km and bigger than moment magnitude Mw=5.0 were used. The results obtained from these two techniques for each station was jointly inverted to determine the 1-D S-wave velocity structure of crust and uppermost mantle. S-wave velocity models along the EAFZ indicate the presence of the low-velocity layers in the upper crust, within the approximately depths of 4-12 km. However, the Conrad discontinuity along the seismic stations was around a depth of ~22 km. Furthermore, the crust-mantle boundary along the EAFZ is about ~44 km depth. Consequently, this study yields the crustal and uppermost mantle S-wave velocity structure compatible with the tectonics of the studied region.

Keywords: Receiver Functions, Rayleigh Wave Dispersion, Joint Inversion, Crustal Structure, Shear Wave Velocity, East Anatolian Fault Zone.

P-Alıcı Fonksiyonları ve Rayleigh Dalgası Grup Hızları'nın Birleşik Ters Çözümü'nden Doğu Anadolu Fay Zonu'nun Kabuk ve Üst Manto Hız Yapısı

Öz

Geçmişten günümüze, yoğun bir deprem aktivitesinin meydana geldiği Doğu Anadolu Fay Zonu (DAFZ) Anadolu ve Arap plakalarının aktif bir sınırıdır. Bu aktivite bölgenin jeodinamik yapısı ile oldukça ilişkilidir. Arap plakasının kuzeye ve Avrasya plakasının güneye hareketinden dolayı, Anadolu plakası saat yönünün tersi doğrultusunda batıya doğru kaçmaya teşebbüs etmektedir. Bu tektonik hareket, önemli tektonik yapıların gelişmesine sebep olmaktadır. Bu aktif plaka hareketleriyle ilişkili olarak, kuzey-doğuda Kuzey Anadolu Fay Zonu (KAFZ) ve güney-batıda Ölü Deniz Fay Zonu (ÖDFZ) ile kesişen DAFZ'nin S-dalgası hız yapısı bölgenin tektonik yapısının yorumlanmasında oldukça önemlidir. Bu çalışmada, DAFZ boyunca sekiz adet geniş-bantlı deprem istasyonundan toplanan verilerin kullanılmasıyla, P-dalgası Alıcı Fonksiyonu ve Rayleigh dalgası grup hızı birleşik ters çözümü yöntemi uygulanmıştır. P-Alıcı fonksiyonları, 3-bileşen geniş-bantlı sismometrelerde kayıt edilen ve her istasyon için ayrı ayrı yaklaşık 80 adet tele-sismik depremin kullanılmasıyla elde edilmiştir. Diğer taraftan, Rayleigh dalgası grup hızı dispersiyon eğrileri

[*] Corresponding Author: hamdialkan@yyu.edu.tr

için odak derinliği 50 km'den küçük ve moment magnitüdü 5.0'dan büyük 21 yerel deprem kullanılmıştır. Her istasyon için bu iki yöntemden elde edilen sonuçlar, kabuk ve üst-mantonun 1-Boyutlu S-dalgası hız yapısını belirlemek için birleşik ters çözüm işlemine tabii tutulmuştur. DAFZ boyunca S-dalgası hız modelleri üst kabukta yani yaklaşık olarak 4-12 km derinliklerinde, düşük hızlı tabakaların varlığına işaret etmektedir. Bununla birlikte, istasyonlar boyunca Conrad süreksizliği 22 km'lik bir derinlik civarındadır. Ayrıca, DAFZ boyunca kabuk-manto geçişi yaklaşık olarak ~44 km derinliğindedir. Sonuç olarak, bu çalışma, incelenen bölgenin tektoniği ile uyumlu kabuk ve en üst manto S-dalgası hız yapısını ortaya koymaktadır.

Anahtar Kelimeler: Alıcı Fonksiyonları, Rayleigh Dalgası Dispersiyonu, Birleşik Ters Çözüm, Kabuk Yapısı, Kesme Dalgası Hızı, Doğu Anadolu Fay Zonu.

1. Introduction

The East Anatolian Fault Zone (EAFZ) is characterized by intensive seismicity and the potential of destructive earthquake occurrences in the instrumental and historical periods. The devastating earthquakes that occurred in the EAFZ with the moment magnitude of Mw≥7.0 have caused severe fatalities and extensive damage (Jamalreyhan et al., 2020). From past to present, previous some strong earthquakes along the EAFZ are 1964 Malatya (Ms=5.7), 1971 Bingöl (Ms=6.9), 1986 Doğanşehir-Malatya (Ms=5.9), 2003 Bingöl (Mw=6.3), 2004 Sivrice (Mw=5.5), and 2010 Kovancılar-Elazığ (Mw=6.3) (Öztürk and Bayrak, 2012; Öztürk, 2017; 2018; Melgar et al., 2020). The last of them is the Elazığ (Sivrice town) earthquake that occurred on January 24, 2020 with moment magnitude Mw=6.8. According to the Republic of Turkey Prime Ministry, Disaster and Emergency Management Authority Presidential of Earthquake Department (AFAD), the Sivrice earthquake resulted in 41 deaths, 1607 injuries, and thousands displaced from their homes. The focal mechanism solution of the Elazığ earthquake is an ENE–WSW striking left-lateral strike-slip fault. According to different national and international institutes, the depth of Elazığ earthquake varies between 8 and 23 km (Cheloni and Akinci, 2020). After the main shock, 995 aftershocks were recorded within 3 days magnitudes ranging from 0.8 to 5.1 (AFAD). After this earthquake, a series of earthquakes with the largest Mw=5.7 occurred in Bingöl (Karlıova town), the northeast of the EAFZ, starting on June 14, 2020 (Figure 1). Considering this intense seismic activity in the region, the relationship between S-wave velocity variations of Earth's crust and the depths of earthquakes is very crucial.

The main goal of this study is to understand the characteristics of the S-wave velocity structure of the study region. In this respect, it was focused on the seismic structure of the crust and uppermost mantle throughout the EAFZ by jointly inverting the teleseismic P-receiver functions and the fundamental mode Rayleigh wave group velocity dispersion curves (Ligorria and Ammon,1999; Julia et al., 2000; Herrmann and Ammon; 2002; Hermann, 2013). The joint inversion provides a good resolution on the S-wave velocity structure, the geological structure, and the different subsurface of boundaries. Using the joint inversion method, it also may provide information about the accurate location of earthquake focal depth con cerning the more robust S-wave velocity model (Agrawal et al., 2015a).

2. Tectonic Setting

The East Anatolia is located in one of the most seismically and tectonically active regions in Turkey, which is a part of the Alp-Himalayan orogenic belt (Dewey et al., 1986; Özer et al., 2019). The East Anatolian region is under the influence of the ongoing collision of the Eurasian Plate and the Arabian Plate since the mid-Miocene period (Dewey et al., 1986). This continental collision is defined by the Bitlis-Zagros Suture Zone (BZSZ) (McClusky et al., 2000; Reilinger et al., 2006) (Figure 1). The BZSZ is a complex continent-continent and continent-ocean collisional boundary and the boundary of mountains uplift (Şengör and Yılmaz, 1981; Öztürk, 2018). The Arabian Plate moving in the north direction at a rate of 15±1 mm/year relatives to the Eurasian Plate (~5 mm/year) and this leads to crustal shortening, thickening, and an average elevation of 2 km above sea level in the region (Reilinger et al., 2006; Gökalp, 2012). The compressional character of the collision zone is reshaped by the major transform faults for instance the North Anatolian Fault Zone (NAFZ) and the EAFZ, due to the westward movement of the Anatolian Plate (20 mm/year) since the middle Miocene (Şengör et al., 1985), where both the EAFZ and the NAFZ accommodate most of the tectonic displacement (Jamalreyhan et al., 2020). The right lateral movement of the NAFZ is about ~27 mm/year, and the left lateral movement of the EAFZ is about ~10 mm/year according to GPS studies (McClusky et al., 2000; Reilinger et al., 2006). Contraction and strike-slip tectonics across the region are still active (Mahatsente et al., 2018).

The NAFZ which has a dextral strike-slip fault system reaches the Marmara Sea in the west and Karliova in the east extending E-W (~1500 km), while the EAFZ is striking SW-NE over about 550 km-length between Karliova triple junction in the northeast, where it joins the NAFZ, and Kahramanmaraş in the southwest where it connects with the Dead Sea Fault Zone (DSFZ) (Bozkurt, 2001; Çoban and Sayıl, 2020). The DSFZ is approximately 1000 km long and a sinistral intraplate strike-slip fault zone extending north-south direction. The DSFZ is considered a plate boundary of transform type and separates the Arabian Plate to the east and the African Plate to the west (Şengör and Yılmaz, 1981). The EAFZ is a sinistral strike-slip fault zone that composes of parallel and obliquely main fault segments northeast-southwest-trending (Öztürk, 2018). The EAFZ consists of six main fault segments. These fault segments are Karlıova-Bingöl, Palu-Hazar Lake, Hazar Lake-Sincik, Çelikhan-Erkenek, Gölbaşı-Türkoğlu, and Türkoğlu-Antakya segments (Yön et al., 2020), caused shallow seismicity and destructive earthquakes at different times (Bayrak et al., 2015; Gülerce et al., 2017; Bayrak et al., 2020).

3. Data Preparation

Figure 1 shows the broadband seismic station distribution. The stations BNGB, KARO, KMRS, and SVRC connected to the Kandilli Observatory and Earthquake Research Institute (KOERI), while stations AKCA, KOVA, MALA, and NARI connected to the AFAD. Detail information on seismic stations was given in Table 1. The regional (Table 2) and teleseismic data (Table 3) in a four-year time interval (2017-2020) were obtained from the European Integrated Data Archive (EIDA)

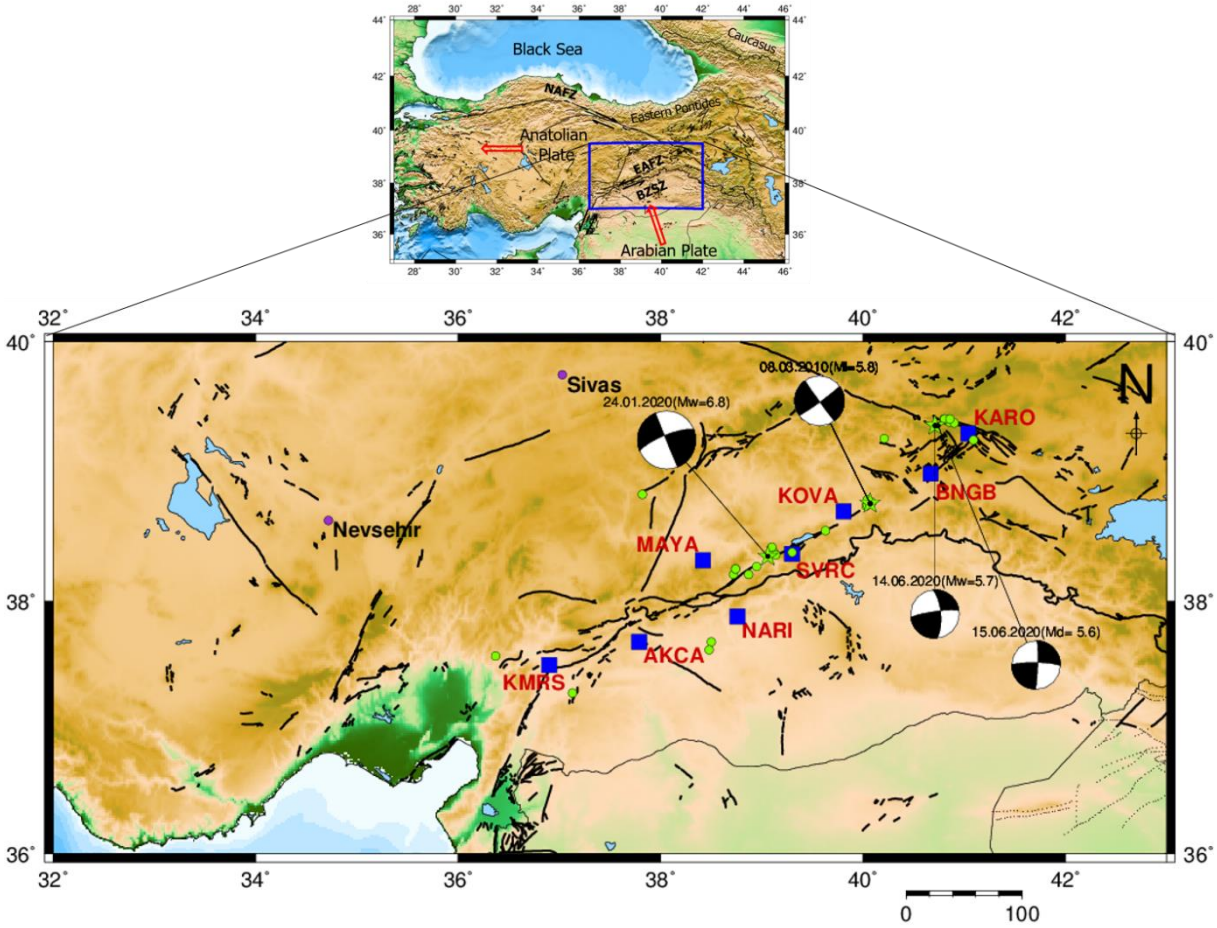

Figure 1. The main tectonic map in the East Anatolian Fault Zone and its surroundings. The blue squares indicate the broadband seismic stations. The green circles and stars represent epicentral distribution greater than Mw=4 after the Sivrice earthquake (24.01.2020) and the fault plane solutions of 4 events with Mw≥5.5 reported in the AFAD earthquake catalog.

(https://www.orfeus-eu.org/data/eida/) and the AFAD (https://tdvms.afad.gov.tr/continuous_data) (Figure 2). In the analysis of the P-receiver functions, the used waveform is from the teleseismic events originated between 30° and 90° from each station generally occurred in the east of the Earth with the moment magnitude Mw≥5.8 and depth h≤100 km. These epicenter distances were chosen to avoid the triplication caused by multiple arrivals in the direct P-wave occurring at distances less than 30° and also complication at distances greater than 90° resulting from the core-mantle boundary (Anand et al., 2018). Similarly, the regional events waveform with moment magnitude Mw≥5.5 and depth h≤50 km that occurred at epicentral distances less than 10° from each station were used for Rayleigh wave group velocity analysis. Based on the signal-to-noise ratio, the best waveform data recorded at each station was seleceted with clear P-wave arrival and Rayleigh wave package. Before the data analysis, the data were firstly detrended, tapered, and bandpass filtered between 0.02 and 0.8 Hz with 5 poles and 2 passes to remove low and high-frequency noise. Then, the instrument response of all data was removed using the pole-zero files. The Seismic Analysis Code software (SAC) was used for the preparation of data (Helffrich et al., 2013).

Table 1. List of broadband stations used in the study region.

No	Station Code	Network Code	Latitude (°)	Longitude (°)	Elevation (m)	Sensor
1	KARO	KO	39.30	41.04	1820	3T
2	BNGB	KO	38.99	40.67	1180	3ESPC
3	KOVA	TU	38.70	39.81	1101	CMG-3T
4	SVRC	KO	38.37	39.30	1680	3T
5	NARI	TU	37.88	38.76	868	CMG-3ESPC
6	MAYA	TU	38.32	38.42	1067	CMG-3ESPC
7	AKCA	TU	37.79	37.68	1067	CMG-3ESPC
8	KMRS	KO	37.50	36.90	590	3T

Table 2. List of regional events used for the Rayleigh wave dispersion curves.

Origin Time	Latitude (°)	Longitude (°)	Depth (km)	Magnitude (Mw)	Region
2017-03-02T11:07:26	37.62	38.43	10.0	5.6	Samsat, Turkey
2017-06-12T12:28:39	38.93	26.36	12.0	6.3	Plomarion, Greece
2017-07-20T22:31:11	36.93	27.41	7.0	6.6	Kos, Greece
2017-11-12T18:18:17	34.91	45.96	19.0	7.3	Halabjah, Iraq
2018-01-11T06:59:30	33.71	45.72	10.0	5.5	Mandali, Iraq
2018-07-22T10:07:27	34.59	46.17	12.0	5.8	Sarpol-e Zahab, Iran
2018-08-25T22:13:25	34.61	46.24	10.0	6.0	Javanrud, Iran
2018-11-25T16:37:32	34.36	45.74	18.0	6.3	Sarpol-e Zahab, Iran
2019-01-06T13:41:59	34.12	45.68	14.0	5.6	Sarpol-e Zahab, Iran
2019-03-20T06:34:27	37.41	29.53	8.0	5.7	Acipayam, Turkey
2019-08-08T11:25:31	37.94	29.70	11.0	5.9	Baklan, Turkey
2019-09-26T10:59:25	40.90	28.15	8.0	5.7	Marmara, Turkey
2019-11-07T22:47:07	37.80	47.58	20.0	5.9	Hashtrud, Iran
2020-01-22T19:22:16	39.07	27.84	5.6	5.6	Kirkagac, Turkey
2020-01-28T15:38:34	35.22	27.89	10.0	5.5	Karpathos, Greece
2020-01-30T01:28:05	35.16	27.88	10.0	5.5	Karpathos, Greece
2020-01-30T11:21:36	35.18	27.78	10.0	5.7	Karpathos, Greece
2020-02-23T05:53:01	38.45	44.42	10.0	5.8	Saray, Turkey
2020-02-23T16:00:31	38.50	44.37	10.0	6.0	Saray, Turkey
2020-06-14T14:24:29	39.42	40.71	10.0	5.9	Yedisu, Turkey
2020-06-15T06:51:31	39.42	40.75	10.0	5.5	Yedisu, Turkey

Table 3. List of teleseismic events used for P-receiver functions analysis.

Origin Time	Latitude (°)	Longitude (°)	Depth (km)	Magnitude (Mw)	Region
2017-02-10T14:03:43	9.91	125.45	15.0	6.5	Philippines
2017-03-14T02:51:16	6.15	92.30	10.0	6.0	India
2017-04-08T07:09:23	13.77	120.94	14.3	5.9	Philippines
2017-04-10T10:38:47	5.68	127.20	13.0	5.8	Philippines
2017-04-11T21:21:00	7.68	124.81	8.3	5.8	Philippines
2017-04-28T20:23:17	5.50	125.07	26.0	6.9	Philippines
2017-05-09T01:54:14	24.45	126.32	10.0	6.0	Japan
2017-07-20T00:11:24	37.42	141.59	31.0	5.8	Japan
2017-07-26T10:32:57	26.90	130.18	12.0	6.0	Japan
2017-08-05T00:30:41	6.11	125.42	76.0	5.8	Philippines
2017-08-08T13:19:49	33.19	103.86	9.0	6.5	China
2017-09-20T16:37:16	37.98	144.66	11.0	6.1	Japan
2017-09-26T20:22:11	40.34	142.34	37.0	5.8	Japan
2017-10-06T07:59:32	37.50	144.02	9.0	6.2	Japan
2017-10-19T09:02:02	28.32	131.21	14.0	5.9	Japan
2017-11-09T07:42:11	32.52	141.44	12.0	6.0	Japan
2017-11-16T09:43:33	32.22	140.55	59.0	5.8	Japan
2017-11-17T22:34:19	29.83	94.98	8.0	6.4	China
2017-11-18T16:07:00	2.46	128.15	8.0	5.8	Indonesia
2017-12-21T03:00:18	29.29	142.65	10.0	5.8	Japan
2018-01-11T18:26:24	18.37	96.07	9.0	6.0	Burma
2018-01-24T10:51:19	41.10	142.43	31.0	6.3	Japan
2018-01-25T01:15:58	8.25	91.77	10.0	5.8	India
2018-02-04T13:56:41	24.16	121.71	12.0	6.1	Taiwan
2018-03-07T04:40:12	45.77	152.38	32.0	5.8	Kuril Islands
2018-04-05T03:53:38	6.83	126.78	34.0	6.0	Philippines
2018-04-15T19:30:43	1.41	126.88	34.0	6.0	Indonesia
2018-05-05T06:19:05	14.57	123.92	18.0	6.1	Philippines
2018-07-07T11:23:50	35.11	140.64	40.0	5.9	Japan
2018-08-10T18:12:07	48.46	154.94	27.0	6.0	Russia
2018-09-05T18:07:59	42.69	141.93	35.0	6.6	Japan
2018-10-09T07:45:11	49.40	156.24	19.0	6.1	Russia
2018-10-10T23:16:02	49.29	156.30	20.0	6.5	Russia

2018-10-23T04:34:58	24.12	122.60	30.0	5.8	Japan
2018-11-04T19:26:03	44.55	145.66	9.0	5.9	Russia
2018-11-29T20:21:44	0.23	97.00	9.9	5.8	Indonesia
2018-12-23T19:32:22	30.41	87.62	10.0	5.8	China
2018-12-29T03:39:09	5.90	126.92	60.2	7.0	Philippines
2019-01-06T17:27:18	2.26	126.76	43.2	6.6	Indonesia
2019-01-08T12:39:30	30.59	131.04	35.0	6.3	Japan
2019-02-08T11:55:07	9.85	126.58	20.0	5.9	Philippines
2019-03-06T00:13:00	8.54	126.92	16.0	5.8	Philippines
2019-03-08T15:06:12	10.38	126.01	30.0	6.0	Philippines
2019-03-24T04:37:35	1.66	126.40	45.0	6.1	Indonesia
2019-04-11T08:18:21	40.41	143.30	18.0	6.0	Japan
2019-04-18T05:01:06	24.04	121.65	20.0	6.1	Taiwan
2019-04-23T20:15:50	28.41	94.56	14.0	5.9	India
2019-04-23T05:37:53	11.75	125.20	56.0	6.4	Philippines
2019-05-31T10:12:32	6.28	126.48	98.7	6.1	Philippines
2019-06-03T05:57:09	0.38	97.72	19.0	5.8	Indonesia
2019-06-18T13:22:19	38.64	139.48	12.0	6.4	Japan
2019-07-07T15:08:40	0.51	126.19	35.0	6.9	Indonesia
2019-08-04T10:23:03	37.76	141.60	38.0	6.3	Japan
2019-08-07T21:28:03	24.48	121.93	20.8	5.8	Taiwan
2019-08-28T23:46:40	41.07	143.00	23.8	5.9	Japan
2019-09-29T02:02:51	5.68	126.55	73.0	6.2	Philippines
2019-10-31T01:11:19	6.91	125.18	10.0	6.5	Philippines
2019-11-14T16:17:40	1.62	126.42	33.0	7.1	Indonesia
2019-11-14T21:12:54	1.54	126.42	23.0	6.0	Indonesia
2019-11-15T01:17:38	1.62	126.35	35.0	5.9	Indonesia
2019-11-16T10:19:13	1.57	126.33	24.0	5.9	Indonesia
2019-11-20T23:50:43	19.45	101.36	10.0	6.2	Thailand
2019-11-23T12:11:15	1.64	132.81	5.0	6.2	Indonesia
2019-12-10T17:05:02	30.73	141.72	11.0	5.8	Japan region
2020-01-07T06:05:19	2.35	96.36	17.0	6.3	Indonesia
2020-01-29T23:46:56	0.71	126.33	27.0	5.8	Indonesia
2020-02-06T13:40:05	5.45	126.57	19.0	6.0	Philippines
2020-03-25T02:49:21	48.96	157.70	57.8	7.5	Russia
2020-03-26T15:38:04	5.57	125.05	59.0	6.1	Philippines
2020-04-05T18:37:10	1.40	126.44	42.0	6.0	Indonesia
2020-04-16T11:45:23	22.80	94.03	10.0	5.9	Myanmar
2020-04-19T20:39:05	38.90	142.00	38.0	6.3	Japan
2020-05-10T23:58:33	36.36	141.13	31.0	5.8	Japan
2020-06-24T19:47:45	35.47	141.07	29.1	5.9	Japan
2020-07-22T20:07:19	33.14	86.86	10.0	6.3	western Xizang
2020-07-27T17:32:45	9.02	126.27	43.4	5.8	Philippines
2020-07-30T00:35:56	30.63	141.77	12.8	5.8	Japan region
2020-09-06T00:21:10	1.67	126.56	30.0	5.9	Indonesia
2020-09-09T07:18:40	4.21	126.64	18.0	5.8	Philippines
2020-09-12T02:44:10	38.76	142.25	32.1	6.1	Japan
2020-09-20T22:13:15	9.22	126.73	10.0	5.8	Philippines

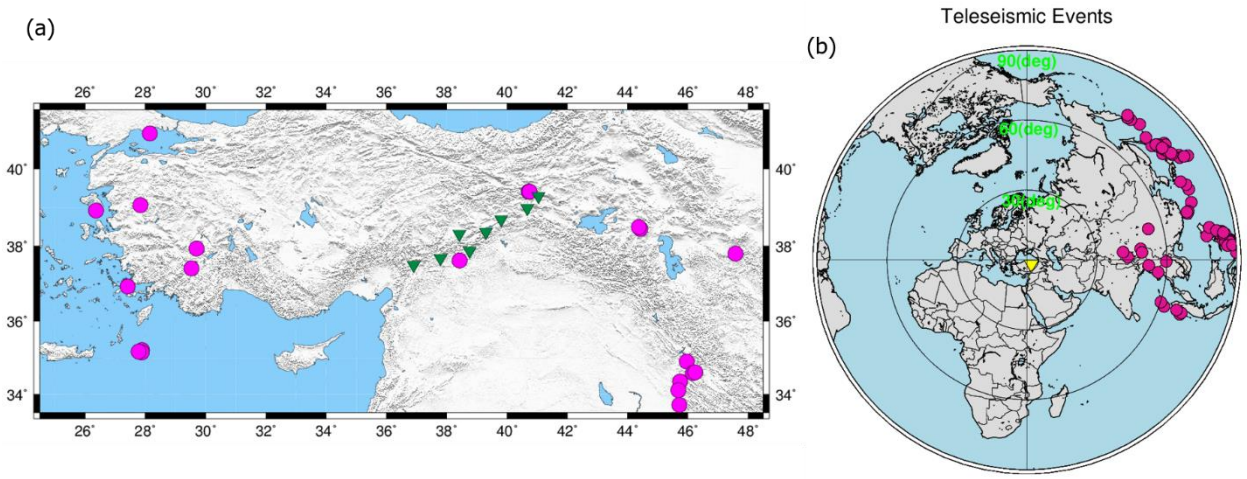

Figure 2. The maps showing the distribution of (a) regional events (4°≤Δ≤10°) for calculation of Rayleigh wave group velocity dispersion curves and (b) teleseismic events (30°≤Δ≤90°) for calculation of P-receiver functions recorded at seismic broadband stations in the East Anatolian region. The green triangles represent the seismic stations in (a), the purple circles show the earthquake epicenters in (a) and (b). The yellow triangle shows the study region in (b).

4. Methods

P-receiver functions and Rayleigh wave group velocity dispersion techniques are widely employed to image the earth's subsurface structures through the recorded seismic response at the three-component broadband stations (Abdul Latiff and Khalil, 2019). The software package Computer Programs in Seismology (Herrmann, 2013) are used for the procedure of these techniques. The program joint96 (Herrmann, 2013) inverts simultaneously both dispersion curves and P-receiver functions stacks. The details of the algorithms were given below.

4.1. P-Receiver Functions

The P-receiver function method was first developed by Langston (1977) and Vinnik (1977) to isolate the near-receiver structure from the source and distant structure. Receiver functions are time-series computed from three-component seismograms and sensitive to the Earth structure below the receiver, which is computed deconvolving the vertical component of the horizontal component (Gonzalez et al., 2012). The main phases of a receiver function generally include P-to-S conversion upon refraction (Ps) and multiple reverberations between surface and discontinuity such as PpPs, PpSs+PsPs, and PsSs arrival at 0 and 25 sec time interval after the first P arrival (Andriampenomanana et al., 2017). Before calculating P-receiver functions, firstly the waveforms in ZNE (vertical, north-south, east-west) are rotated vertical components into radial and tangential components (ZRT system) using back azimuth information. The time window of components is cut to a length of 90 s (10 s before P arrival and 80 s after P arrival). After rotation of the three-component data, radial P-receiver functions are obtained by the iterative time-domain deconvolution technique (Ligorria and Ammon, 1999) with 600 iterations. Iteration number means an improved fit between two iterations (Ammirati et al., 2015). In the process of calcuation radial receiver functions, the vertical-component seismogram is subtracted from the radial-component seismogram, and the procedure is repeated to estimate other spike lags and amplitudes. With each additional spike in the receiver function, the misfit between the vertical and receiver-function convolution and the radial-component seismogram is reduced, and the iteration stops when the reduction in misfit with additional spikes becomes insignificant (0.01 per cent) (Ligorria and Ammon, 1999). In the deconvolution process, the Gaussian filter ($G(w)=\exp(-w^2/4a^2)$), where "w" is the angular frequency and "a" is a filter width parameter, is applied to remove high-frequency noise. The parameter "a" controls the resolution of layer thickness and frequency content (Agrawal et al., 2015b). Gaussian filter parameter only uses 1.0 and 2.5 to limit crust and uppermost mantle. The radial component of the P-receiver function is presented as a function of back-azimuth for each station (Figures 5-12). Then, for each station, all deconvolved P-receiver functions are stacked to increase the signal-to-noise ratio and enhance the quality of P-to-S converted phases by using the SAC (Helffrich et al., 2013).

4.2. Rayleigh Wave Group Velocities

Surface wave modeling is the most sensitive to shallow S-wave velocities of the crust and upper mantle and allows an alternative strategy for finding accurate velocity models associated with receiver functions (Agrawal et al., 2015b). Also, surface wave group velocities provide information on the long-wavelength vertical averages of the S-wave structure (Badawy et al., 2018). Rayleigh waves are generally easy to isolate on the vertical component of a seismogram. For this reason, the fundamental-mode Rayleigh wave group velocities, in the period range from 5 to 45 s, are computed by using multiple filter technique (MFT) (Dziewonski et al., 1969) and phase match filtering (PMF) (Goforth and Herrin, 1979), which is isolated fundamental mode, (Herrmann, 2013). The MFT applies a narrow bandpass Gaussian filter to the broad-band, vertical-component, displacement seismogram over many different periods (Herrmann, 2013). The group velocity dispersion curves are manually picked from the maximum amplitudes in a plot of group velocity (km/s) versus period (s). To minimize the influence of lateral heterogeneity along the wave propagation path (Çınar and Alkan, 2017), the group velocity dispersion curves obtained for each station are averaged statistically (Figures 3 and 4), used in the joint inversion.

4.3. Joint Inversion

Jointly inverting receiver functions with Rayleigh wave group velocity dispersion data helps to reduce nonuniqueness because the dispersion data help to constrain absolute S-wave velocity values and receiver functions primarily sensitive to

large wave gradients (Gilligan et al., 2014). In this study, the joint inversion procedure developed by Julia et al. (2000) was used to obtain the S-wave velocity models for each station. This technique performs using an iterative damped least-squares algorithm by minimizing the objective function, defined by

the trade-off between resolution and stability (Julia et al., 2000), is generally fixed at σ =0.4-0.5 after testing several damping parameters. The parameter p, which is the influence of either data on the minimization, has been chosen by trial and error to be in the range from 0.1 to 1.0, so that the resulting models have the best percentage of fit, and dispersion curves consistent. If the p-value is chosen as 0, it is mean that includes only receiver functions, or if the p-value is chosen as 1, inversion includes only Rayleigh wave data (Julia et al., 2000). For the maximum contribution of receiver functions and Herrmann and Ammon (2002). The time window of the stacked P-receiver function for joint inversion is set to -5 and +20 sec. A damping parameter is necessary to avoid rapid and improbable velocity variations with depth (Ammirati et al., 2015). The modest damping parameter in the inversion, which is balanced dispersion curves, different p values are tested such as 0.2, 0.3, 0.4, 0.5, 0.6, 0.7, and 0.8. Finally, it is found the value of 0.4 and 0.5 for a good fit of both data sets. The weights of the upper crust layers are chosen as 0.8 and the weights are 0.4 for the lower crust and the upper mantle layers. This choice has been adopted on account of the available independent information. The initial model in this study consists of Litho1.0 (Pasyanos et al., 2014) and AK135-F continental model (Kennett et al., 1995) up to 100 km depth. The layers have 2 km thick at a depth of 50 km, and 5 km from 50 km and 100 km depth.

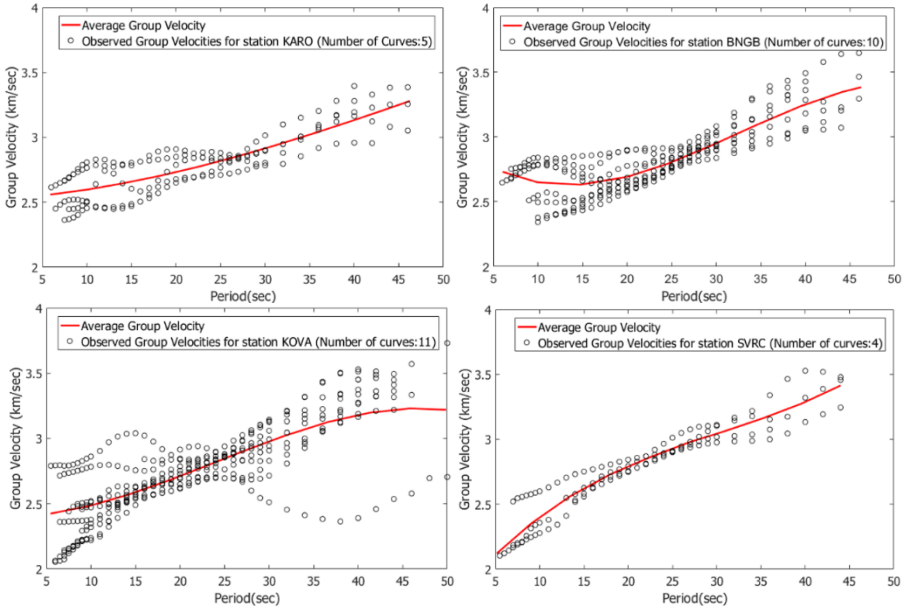

Figure 3. The Rayleigh wave average (solid red lines) and observed (black dotted) group velocity curves for stations KARO, BNGB, KOVA and SVRC.

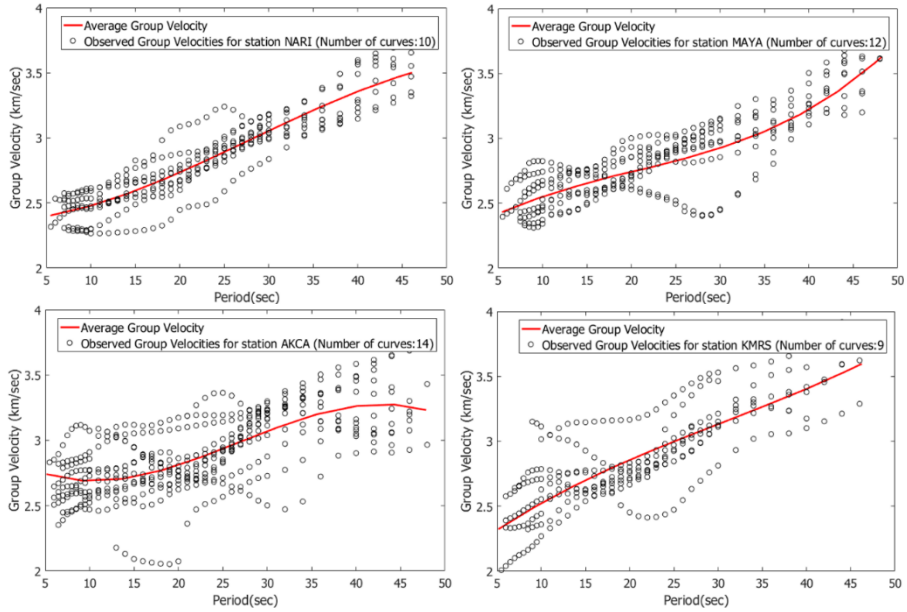

Figure 4. The Rayleigh wave average (solid red lines) and observed (black dotted) group velocity curves for stations NARI, MAYA, AKCA and KMRS.

5. Results and Discussion

P-receiver functions are primarily sensitive to shear wave velocity contrasts in layered structures while Rayleigh wave group velocity dispersion curves are sensitive to averaged shear wave velocities (Agrawal et al., 2015b). Combining the average

Rayleigh wave dispersion curve and P-receiver functions stacks can effectively overcome the resolution gap associated with individual data sets (Desphande and Mohan, 2016). In this section, the results of joint inversion were interpreted in the northeast-southwest direction, and results were compared with previous studies. In the interpretation of P-receiver functions waveforms, the ray diagram of Ammon et al. (1990) is used, showing the ray paths of the major P-to-S converted phases and associated multiples (Akpan et al., 2016; Abdul Latiff and Khalil, 2019).

For the station KARO located in the northeast of the study region, the number of P-receiver functions for the stack was taken as 21, and the number of Rayleigh wave group velocity curves is 5 for the average curve (Figure 5). After the first P arrival, the Ps phase (Moho converted phase) appears at ~5 s. Then, PpPs phase at around 16 s and PpSs + PsPs phase at around 21 s (the reflections from the Moho and the Earth's surface) are observed in P-receiver functions (Figures 5a and 5c) (Akpa et al., 2016). The average Rayleigh wave group velocity curve was obtained 6 to 46 s (Figure 5b). According to the S-wave velocity model (Figure 5d), station KARO has an estimated crustal thickness of ~43 km (Vs=4.22 km/s). The Conrad discontinuity (upper crust-lower crust boundary or transition granitic-basaltic transition (Abdelwahed et al., 2013) can be interpreted at approximately 16 km (Vs=3.64 km/s). The low-velocity zone (LVZ) in the upper crust (Vs=~3.08 km/s) is between 4 and 16 km.

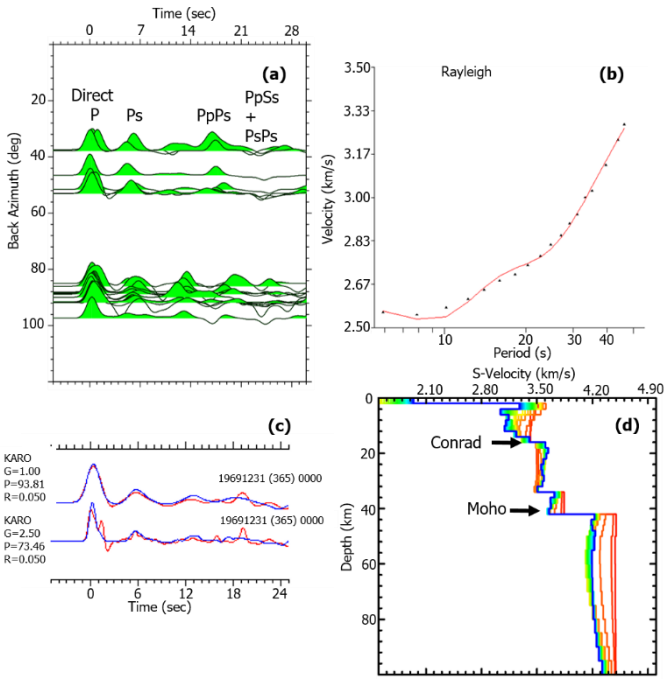

Figure 5. The results from joint inversion for station KARO (a) 21 P-receiver function waveforms sorted by Back Azimuth (b) Average Rayleigh wave group velocity curve (black circles) and its prediction (red solid curve) (c) Receiver functions stacks (blue curve) and their predictions (red curve). G, P, and R are the Gaussian filter parameter, the percentage of fit, and the average ray parameter (sec/km) at the left of each trace, respectively. (d) After 30 iterations, the inverted S-wave velocity model (the red line is the initial model and the blue line is the final model).

For the station BNGB, the number of P-receiver functions was considered as 48 for the stack, and the number of Rayleigh wave group velocity curves is 10 for the average curve (Figure 6). The results of P-receiver function at station BNGB show a coherent Ps converted wave arrival from the Moho boundary at ~5 s. At the later time, the PpPs phase can be seen clearly at 17 s with weak PpSs +PsPs multiple at 21 s (Figure 6a and 6c). The periods of average Rayleigh wave group velocity curve is between 6 and 46 s (Figure 6b). According to the S-wave velocity model (Figure 6d), the station BNGB has Moho depths of ~44 km (Vs=4.34 km/s), and Conrad discontinuity appears as ~18 km (Vs=3.60 km/s). The LVZ at the depth of 10±4 km was observed in the upper crust (Vs=~3.0 km/s).

For the station KOVA, the number of P-receiver functions was used as 37 for the stack, and the number of Rayleigh wave group velocity curves is 11 for the average curve (Figure 7). Although the Ps phase does not observe clearly in the P-receiver functions after the first P phase, it may be said to be arriving around 8 seconds. This may be due to the percentage of fit not being too high. Similarly, the PpSs+PsPs phase is also missing (Figures 7a and 7c). The average Rayleigh wave group velocities are in the period range between 5 and 45 s (Figure 7b). The crustal thickness beneath the station KOVA is ~44 km (Vs=4.27 km/s) (Figure 7d). It can be said that the Conrad discontinuity is around 16 km (Vs=3.68 km/s). The low-velocity layers were detected in the depth of 4-8 km prominently (Vs=~2.88 km/s).

For the station SVRC, the number of P-receiver functions was taken as 20 for the stack, and the number of Rayleigh wave group velocity curves is 4 for the average curve (Figure 8). The Ps phases could not be observed crudely due to data quality is not very high. However, the Ps phase from the Moho and PpPs phase can be interpreted around 5 s and 14 s, respectively (Figures 8a and 8c). The period range is from 5 to 44 s in station SVRC (Figure 8b). The velocity structure for station SVRC in Figure 8d shows the Moho depth of 45 km (Vs=4.36 km/s) and the Conrad depth of ~18 km (Vs=3.70 km/s). The upper crust is characterized by low velocities, appeared the LVZ at the depth of 4 km (~2.54 km/s).

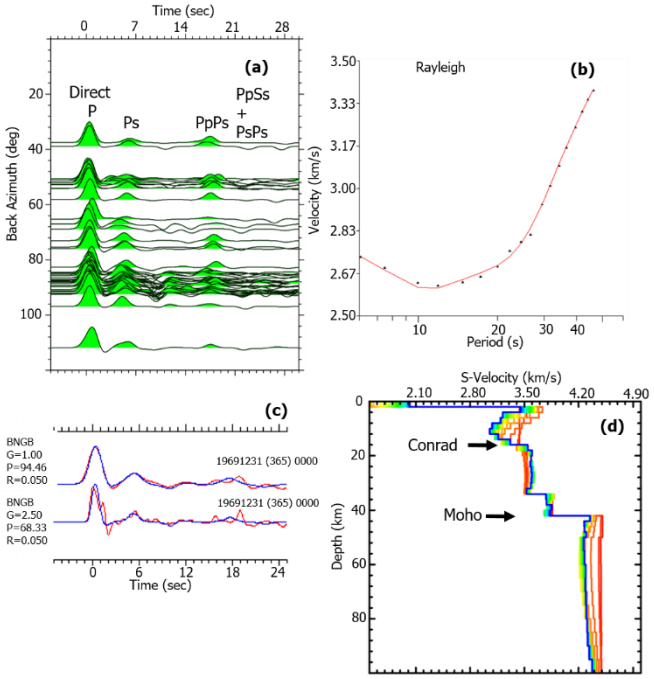

Figure 6. The results from joint inversion for station BNGB (a) 48 P-receiver Function waveforms sorted by Back Azimuth (b) Average Rayleigh wave group velocity curve (black circles) and its prediction (red solid curve) (c) Receiver functions stacks (blue curve) and their predictions (red curve). G, P, and R are the Gaussian filter parameter, the percentage of fit, and the average ray parameter (sec/km) at the left of each trace, respectively. (d) After 30 iterations, the inverted S-wave velocity model (the red line is the initial model and the blue line is the final model).

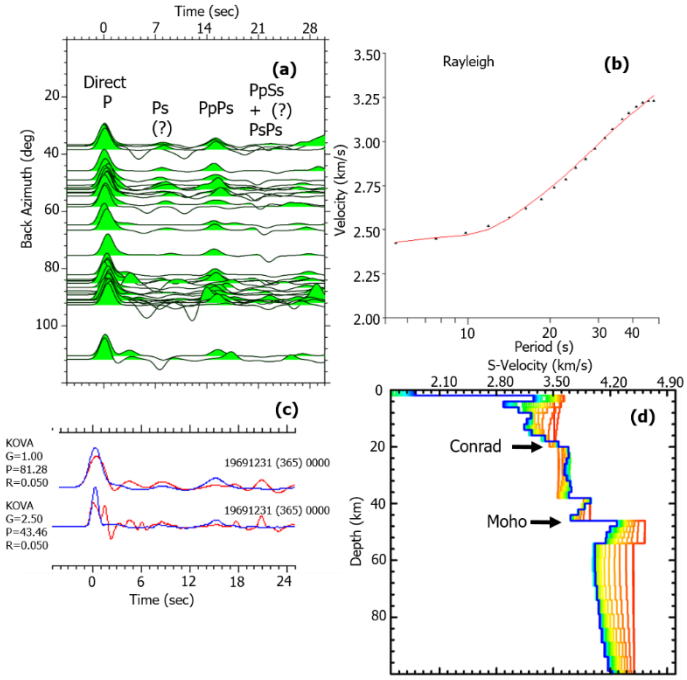

Figure 7. The results from joint inversion for station KOVA (a) 37 P-receiver Function waveforms sorted by Back Azimuth (b) Average Rayleigh wave group velocity curve (black circles) and its prediction (red solid curve) (c) receiver Functions stacks (blue curve) and their predictions (red curve). G, P, and R are the Gaussian filter parameter, the percentage of fit, and the average ray parameter (sec/km) at the left of each trace, respectively. (d) After 30 iterations, the inverted S-wave velocity model (the red line is the initial model and the blue line is the final model).

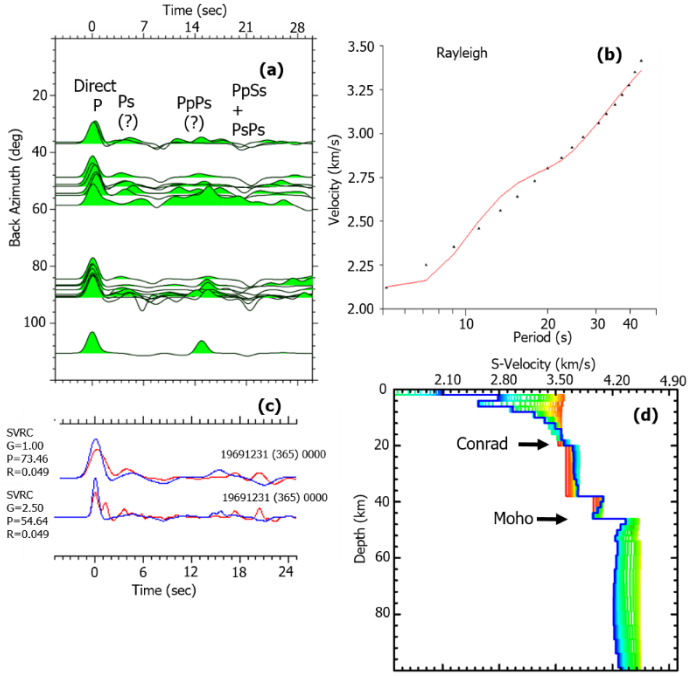

Figure 8. The results from joint inversion for station SVRC (a) 20 P-receiver Function waveforms sorted by Back Azimuth (b) Average Rayleigh wave group velocity curve (black circles) and its prediction (red solid curve) (c) Receiver functions stacks (blue curve) and their predictions (red curve). G, P, and R are the Gaussian filter parameter, the percentage of fit, and the average ray parameter (sec/km) at the left of each trace, respectively. (d) After 30 iterations, the inverted S-wave velocity model (the red line is the initial model and the blue line is the final model).

For the station NARI, the number of P-receiver functions was considered as 39 for the stack, and the number of Rayleigh wave group velocity curves is 10 for the average curve (Figure 9). The Ps and PpSs+PsPs phases are detected at ~4 s and ~17 s, respectively, although the PpPs phase is not visible (Figures 9a and 9c). The periods of average Rayleigh wave group velocity curve is obtained from 5 to 46 s (Figure 9b). The inversion results show the Moho at 44 km with Vs=4.38 km/s and Conrad at ~16 km with Vs=3.60 km/s (Figure 9d). The LVZ at the depth of 4-8 km was observed in the upper crust (Vs=~2.97 km/s).

For the station MAYA, the number of P-receiver functions was used as 43 for the stack, and the number of Rayleigh wave group velocity curves is 12 for the average curve (Figure 10). After the first P arrival, the Ps phase from the Moho appears at ~5 s. After that, the PpPs phase at ~14 s and PpSs + PsPs phases at around 21 s were observed in P-receiver functions (Figures 10a and 10c). The period of the average Rayleigh wave group velocity dispersion curve is in the range of 5-45 s (Figure 10b). According to the S-wave velocity model in Figure 10d, the thickness of crust is 44 km (Vs=4.33 km/s) and the Conrad transition is ~16 km (Vs=3.57 km/s). Like other joint inversion results, the LVZ was observed in station MAYA at the depth of 4-16 km (Vs=~2.89 km/s).

For the station AKCA, the number of P-receiver functions was taken as 59 for the stack, and the number of Rayleigh wave group velocity curves is 14 for the average curve (Figure 11). The P to S converted phase Ps which delineates the crust-upper mantle interface is nearly observed at 4-5 s. The PpPs and PpSs+PsPs phases were detected at about 13 s and 19 s, respectively (Figure 11a and 11c). The averaged group velocity curve of the fundamental mode of Rayleigh wave is estimated for the period range from 5 to 44 s (Figure 11b). Conrad discontinuity is found at ~18 km depth (Vs=3.57 km/s) and the Moho discontinuity is at about ~42 km (Vs=4.28 km/s) (Figure 11d). The low-velocity layers were noticed with S-wave velocity ~3.12 km/s between 6 and 14 km depth.

For the station KMRS located in the southwest of the study region, the number of P-receiver functions was considered as 27 for the stack, and the number of Rayleigh wave group velocity curves is 9 for the average curve (Figure 12). Similar to the results of station AKCA, at KMRS station after deconvolving P-receiver functions, it was found the converted Ps phase at about 5 s, PpPs phase at about 13 s, and PpSs+PsPst phase about 18 s (Figure 12a and 12c). The average Rayleigh wave group velocity is between periods of 5 and 44 s (Figure 12b). In Figure 12d, the Moho discontinuity was marked at approximately 42 km (Vs=4.48 km/s) and the Conrad discontinuity was observed 16 km depth (Vs=3.66 km/s). The LVZ was found at the depth of 8±4 km (~2.83 km/s) in the upper crust.

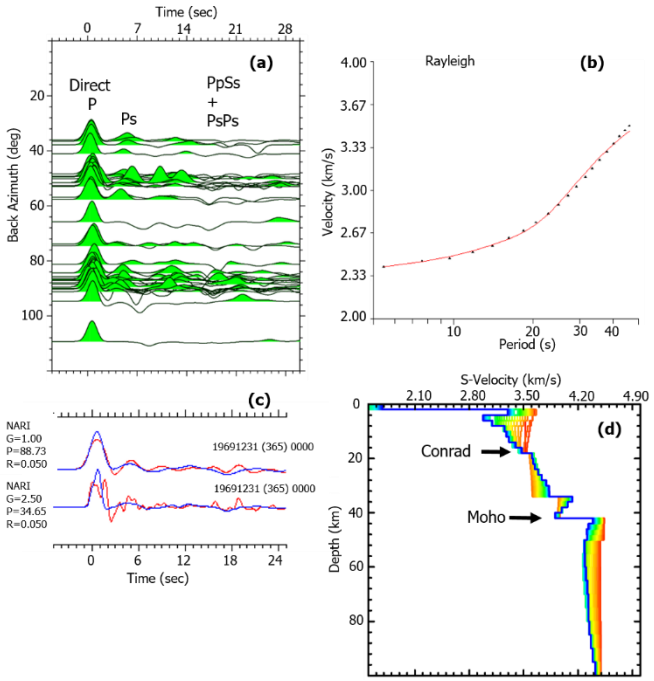

Figure 9. The results from joint inversion for station NARI (a) 39 P-receiver Function waveforms sorted by Back Azimuth (b) Average Rayleigh wave group velocity curve (black circles) and its prediction (red solid curve) (c) Receiver functions stacks (blue curve) and their predictions (red curve). G, P, and R are the Gaussian filter parameter, the percentage of fit, and the average ray parameter (sec/km) at the left of each trace, respectively. (d) After 30 iterations, the inverted S-wave velocity model (the red line is the initial model and the blue line is the final model).

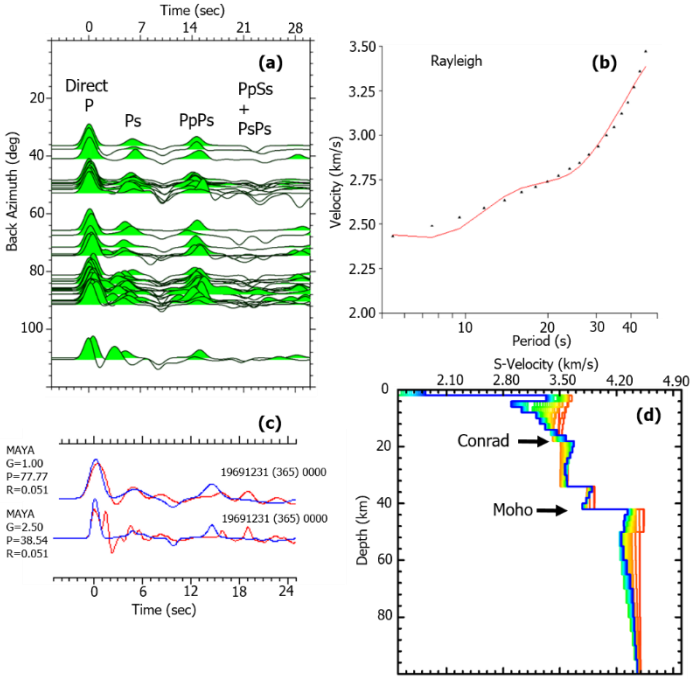

Figure 10. The results from joint inversion for station MAYA (a) 43 P-receiver Function waveforms sorted by Back Azimuth (b) Average Rayleigh wave group velocity curve (black circles) and its prediction (red solid curve) (c) Receiver functions stacks (blue curve) and their predictions (red curve). G, P, and R are the Gaussian filter parameter, the percentage of fit, and the average ray parameter (sec/km) at the left of each trace, respectively. (d) After 30 iterations, the inverted S-wave velocity model (the red line is the initial model and the blue line is the final model).

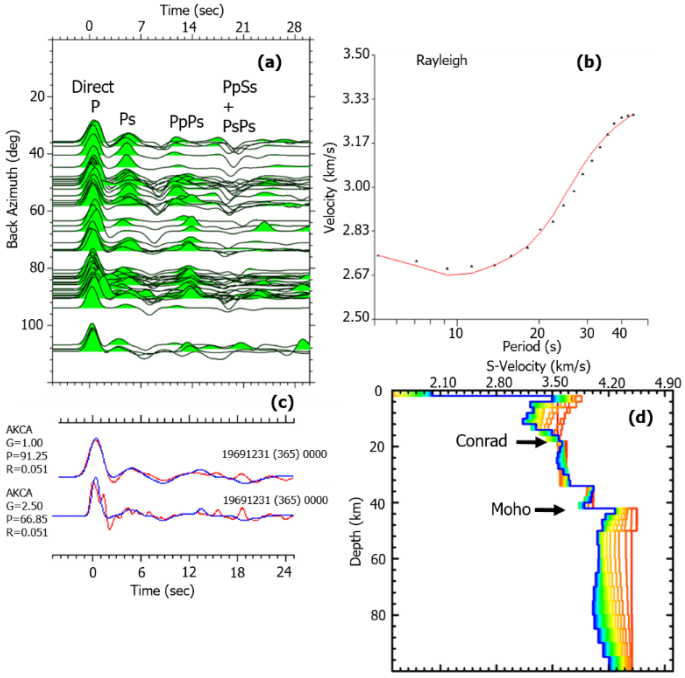

Figure 11. The results from joint inversion for station AKCA (a) 59 P-receiver Function waveforms sorted by Back Azimuth (b) Average Rayleigh wave group velocity curve (black circles) and its prediction (red solid curve) (c) Receiver functions stacks (blue curve) and their predictions (red curve). G, P, and R are the Gaussian filter parameter, the percentage of fit, and the average ray parameter (sec/km) at the left of each trace, respectively. (d) After 30 iterations, the inverted S-wave velocity model (the red line is the initial model and the blue line is the final model).

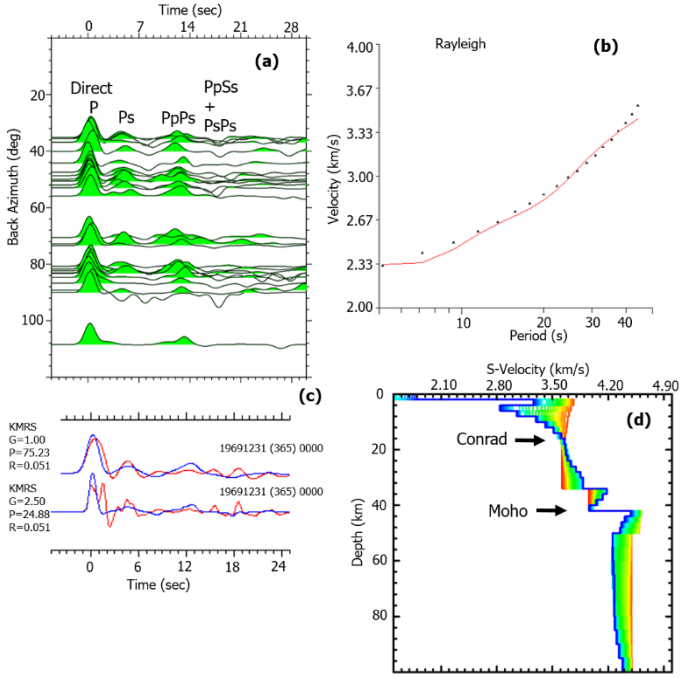

Figure 12. The results from joint inversion for station KMRS (a) 27 P-receiver Function waveforms sorted by Back Azimuth (b) Average Rayleigh wave group velocity curve (black circles) and its prediction (red solid curve) (c) Receiver functions stacks (blue curve) and their predictions (red curve). G, P, and R are the Gaussian filter parameter, the percentage of fit, and the average ray parameter (sec/km) at the left of each trace, respectively. (d) After 30 iterations, the inverted S-wave velocity model (the red line is the initial model and the blue line is the final model).

In this section, the results of this study were compared with literature studies achieved in and around the EAFZ. In the S-wave velocity models, the presence of low-velocity layers in the upper crust was clearly observed varying between 4-14 km depths, and S-wave velocities change from 2.5 km/s to 3.1 km/s. The Conrad discontinuity obtained from S-wave velocity models (Figures 5-12), which is the boundary of the upper and lower crust, was observed at a depth of approximately 20 km (Vs=~3.65 km/s). This result is consistent with previous studies. The crust-upper mantle boundary is around 44 km (Vs=4.33 km/s) from the northeast to the southwest. The upper mantle S-wave velocity variations from the joint inversion results of each station are generally similar and have uniform change (Figures 5-12). Zor et al. (2003) observed the low-velocity layers at the

depth of 15-25 km associated with the presence of the young basaltic volcanics and the crustal thickness of 45 km (Vs=~3.7 km/s) in the northeast of EAFZ. Al-Lazki et al. (2004) mapped Pn-velocities to explain the upper mantle dynamics in the junction of the Arabian, Eurasian and African plates. They found the low Pn-velocities (≤ 8 km/s) in and around Eastern Turkey, associated with the latest stage of intense volcanism has been started since the late Miocene. Angus et al. (2006) determined crust and upper-mantle seismic discontinuities in the northwest of EAFZ. The crustal low-velocity zone was observed in the station KRLV at ~20 km depth, and may represent a pocket of partial melt in the middle crust and quaternary volcanic centers. The estimated Moho was roughly 35 km between 37.0–39.0 °N and 38.0–42.0 °E. Bektaş et al. (2007) recommended the Curie point depths over the region of the East Anatolia varied from 13 to 23 km. These depths, which may be associated with the brittle-ductile transition around 20 km depth, corresponded to magnetite-dominated mineralogy with the Curie point of 580 °C and high-temperature depths. Using the data of the Eastern Turkey Seismic Experiment Project (ETSE), Özacar et al. (2010) calculated the Moho depth between 40 and 45 km in the northeast of EAFZ. Bakirci et al. (2012), using the surface wave tomography algorithm, observed slow velocity anomalies that were related to widespread Neogene and Holocene volcanism. Gökalp (2012), using the data of ETSE just like Özacar et al. (2010), revealed widespread low-velocity anomalies at varying depths of the upper crust of the East Anatolian plateau. Based on the receiver functions analysis, Tezel et al. (2013) interpreted the crustal structure of Turkey. According to their results, the Moho varied between 40 and 49 km with an average S-wave velocity of 4.3 km/s in the East Anatolian region. Vanacore et al. (2013) detected that the Moho depth around the EAFZ was between 35-40 km. Warren et al. (2013) obtained the low-shear velocity anomalies (≤3.5 km/s) from 5 to 20 km depth interval beneath the EAFZ. These anomalies were associated with the Neogene volcanics and the continued presence of hot rock at shallower depths. Delph et al. (2015) found that low-shear velocities in the upper crust (between 10 and 25 km) stemmed from the presence of fluids in the fault zone and rheological weakening of the lower crust in the Eastern Anatolia. According to velocity sections, Moho depth was nearly 45 km in the same region. Their region corresponds to the vicinity of the station MAYA and NARI in this study. Kind et al. (2015) found that the lithosphere-asthenosphere boundary changed between 80 and 100 km depth beneath Turkey. In the study of Türkoğlu et al. (2015), the EAFZ was underlain low resistivity zone that extended into the crust (between 10 and 20 km depths). The low resistivity likely indicated a region of elevated fluid content, most likely partial melt. Based on the three-dimensional joined inversion of topography, gravity, and geoid data, Motavalli-Anbaran et al. (2016) obtained that Moho varied from 37±3 km in the Bitlis suture to 45±3 km in the East Anatolian plateau. Also, the strongly thinned lithosphere (100±10 km) was observed in the East Anatolian Accretionary Complex. Lü et al. (2017) studied Pn velocity changes with the seismic tomography algorithm from eastern Europe to western China. They calculated low Pn velocities (~8.0 km/s) around the Dead Sea Fault Zone, caused by hot material upwelling in this rift zone. Oruç et al. (2017) found that average depths of the Lithosphere-Asthenosphere boundary, Moho, and Conrad (brittle upper crust-ductile lower crust) in the EAFZ are 85 km, 40 km, and 18 km, respectively. Çırmık (2018) observed high heat flow, high seismicity which was occurred in the upper crust (~20 km depth), shallower curie point depth, and the low Vs values (~3.50 km/s) along the EAFZ. These results showed the high geothermal potential of the region and verify the lateral brittle-ductile transition at the depth of ~16 km. Mahatsente et al. (2018) constructed the lithospheric mantle profiles along 38 to 44°E. According to their profiles, lithospheric depth was thinner ~70 to ~90 km along the EAFZ. This was associated with the delamination of the Anatolian lithosphere and may be asthenospheric flow. Ozer et al. (2019) applied the local earthquake tomography method in the EAFZ and determined four main seismic crustal layers down to 40 km. The upper crust (0-8 km) had low-velocity anomalies associated with sedimentary units. Conrad discontinuity was detectable at 20 km depth, while Moho depth was computed at depth of ~40 km in the region. The results of Salah and Şahin (2019) about the SE Anatolia showed that the low-velocity zones and high Vp/Vs ratios at the depth interval of 10 and 22 km were more widely distributed beneath the active fault segments and the region had generally thick sedimentary cover. The high values were related to the possible existence of over-pressurized fluids in the crust, which can trigger large crustal earthquakes along with the western part of the EAFZ. In the end, the crust and most-upper mantle structure along with the EAFZ is searched at a regional scale and interpreted in this study. When compared with previous seismological studies, models obtained from present study generally agree with estimates of S-wave velocity values and discontinuity depths from previously published receiver functions, seismic tomography and surface wave dispersion studies. The LVZ is saliently proposed beneath the upper crust and reflects the depth of earthquakes occured, and the Moho velocities are consistent with continental values.

6. Conclusions

In this study, the S-wave velocity structure was examined up to 100 km depth by joint inversion of stacked P-receiver functions and Rayleigh wave group velocity dispersion data. All S-wave velocity models show a thin layer of relatively low velocity (2.8 km/s<Vs<3.1 km/s) between depths of approximately 4 and 16 km (Figure 13). It may be attributed that existing highly fractured rock and fault gouge along the EAFZ can generate an LVZ in the upper crustal portion of the studied area, where earthquakes are densely accumulated within this LVZ. In Figure 13, the cross-section in the northeast-southwest direction was obtained from the inverted S-wave velocity models of each station. The cross-section shows that the earthquakes, whose focal depths are from the surface to 50 km depth, located in the EAFZ. It can be seen that the number of earthquakes, occurred in the region, diminishes swiftly after 20 km depth. The compatibility between the seismicity of the region and the Earth's discontinuities associated with the S-wave velocity is very significant and essential for better seismic characterization such as focal mechanism determination and source parameter. According to the AFAD earthquake catalog, the regional events that are greater than M≥4.0 and time interval are 2000-2020 generally occur between 10 and 20 km depths. The depth-distribution of earthquake hypocenters indicates that the brittle-ductile transition along the EAFZ corresponds to a depth of approximately 20 km in which variation of S-wave velocity increases from 3.1 to 3.5 km/s. This shallow seismicity has mainly dominated the left-lateral strike-slip motion of the EAFZ segments. The Conrad discontinuity obtained in this study has a good correlation with the earthquake focal depths and regional seismicity. It is clear that average Moho depths were

obtained 43±2 km along with the EAFZ. Below the Moho discontinuity, shear velocities in the uppermost mantle vary for similar trends. Finally, the new findings shed new light on detailed information for studying the crust-uppermost mantle structural features of the EAFZ.

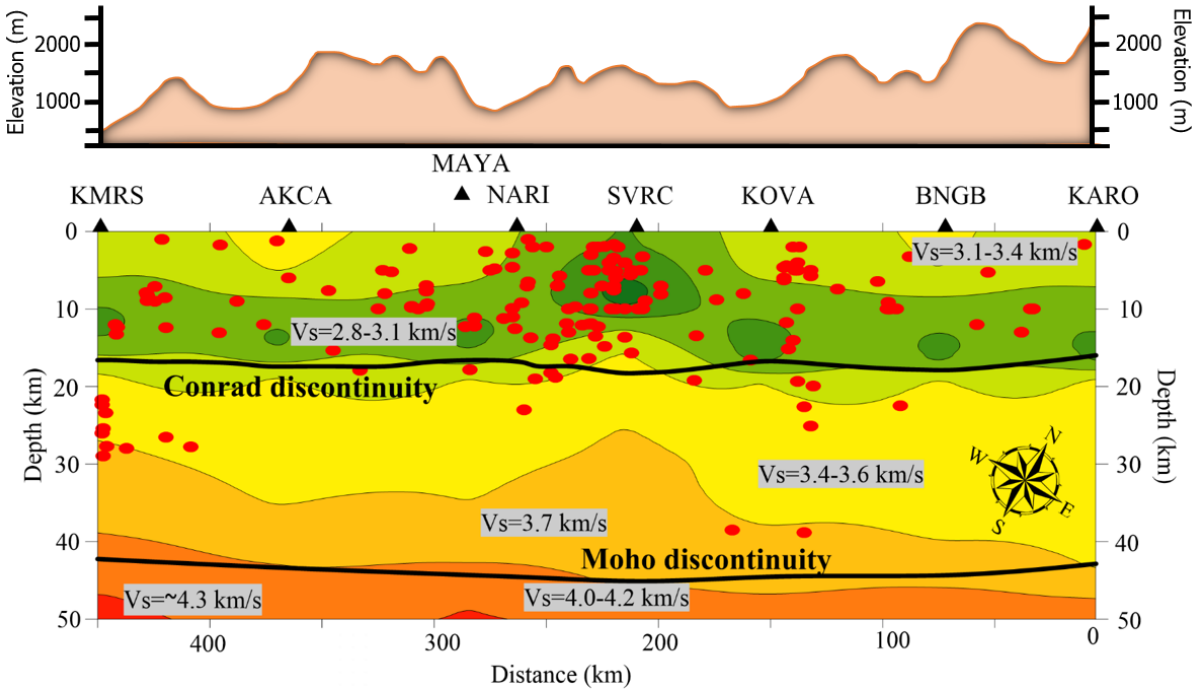

Figure 13. The 2-D crustal shear wave velocity cross-section beneath the EAFZ with the topography map. Black triangles represent broadband seismic stations, red dots represent the distribution of earthquake hypocenters that occurred between 2000 and 2020 with magnitudes greater than 4.0. The earthquake catalog information was taken from the AFAD.

7. Acknowledge

I would like to thank R.B. Herrmann and C.J. Ammon for making their codes (Computer Programs in Seismology, Version 3.30) available for the computation of receiver functions and surface wave dispersion. I would like the editor and reviewers for their valuable suggestions and constructive comments for improving the manuscript. Also, I am grateful to the EIDA and the AFAD for providing the broadband seismic data. Some figures were prepared by using Generic Mapping Tools (GMT) (Wessel et al., 2013).

References

Abdelwahed, M.F., El-Khepy, S., Qaddah, A. (2013). Three-dimensional strcuture of Conrad and Moho discontinuities in Egypt. *Journal of African Earth Sciences*, 85, 87–102.

Abdul Latiff, A.H., Khalil, A.E. (2019). Crustal thickness and velocity structure of Malay Peninsula inferred from joint inversion of receiver functions and surface waves dispersion. *Journal of Asian Earth Sciences*, 169, 105–116.

Agrawal, M, Pulliam, J., Sen, M.K., Dutta, U., Pasyanos, M.E., Mellors, R. (2015a). Crustal and uppermost mantle structure in the Middle East: assessing constraints provided by jointly modelling Ps and Sp receiver functions and Rayleigh wave group velocity dispersion curves. *Geophys. J. Int.*, 201, 783–810.

Agrawal, M., Pulliam, J., Sen, M.K., Gurrola, H. (2015b). Lithospheric structure of the Texas-Gulf of Mexicpassive margin from surface wave dispersion and migrated Ps receiver functions. *Geochem. Geophys. Geosyst.*,16, 2221–2239.

Akpan, O., Nyblade, A., Okereke, C., Oden, M., Emry, E., Julià, J. (2016). Crustal structure of Nigeria and Southern Ghana, West Africa from P-wave receiver functions. *Tectonophysics*, 676, 250–260.

Al-Lazki, A., Sandvol, E., Seber, D., Barazangi, M., Türkelli, N., Mohamad, R. (2004). Pn tomographic imaging of mantle lid velocity and anisotropy at the junction of the Arabian, Eurasian and African Plates. *Geophysical Journal International*, 158, 1024–1040.

Ammirati, J.B., Patricia, A., Beck, S. (2015). A lithospheric velocity model for the flat slab region of Argentina from joint inversion of Rayleigh wave phase velocity dispersion and teleseismic receiver functions. *Geophys. J. Int.*, 202, 224–241.

Ammon, C.J., Randall, G.E., Zandt, G. (1990). On the non-uniqueness of receiver function inversions. *J. Geophys. Res.*, 95, 15303–15318.

Andriampenomanana, F., Nyblade, A.A., Wysession, M.E., Durrheim, R.J., Tilmann, F., Julia, J., Pratt, M.J., Rambolamanana, G., Aleqabi, G., Shore, P.J., Rakotondraibe, T. (2017). The structure of the crust and uppermost mantle beneath Madagascar. *Geophys. J. Int.*, 210, 1525–1544.

Angus, D., Wilson, D., Sandvol, E., Ni, J.F. (2006). Lithospheric structure of the Arabian and Eurasian collision zone in eastern Turkey from S-wave receiver functions. *Geophysical Journal International*., 166, 1335–1346.

Badawy, A., Hegazi, M., Gaber, H., Korrat, I. (2018). Crustal structure of northern Egypt from joint inversion of receiver functions and surface wave dispersion velocities. *J Seismol*, 22, 697-719.

Bakirci, T., Yoshizawa, K., Ozer, M.F. (2012). Three-dimensional S-wave structure of the upper mantle beneath Turkey from surface wave tomography. *Geophysical Journal International.*, 190(2), 1058–1076.

Bektaş, Ö., Ravat, D., Büyüksaraç, A., Bilim, F., Ateş, A. (2007). Regional geothermal characterisation of East Anatolia from aeromagnetic, heat flow and gravity data. *Pure and Applied Geophysics*., 164, 975–998.

Bozkurt, E. (2001). Neotectonics of Turkey-a synthesis. *Geodyn Acta*., 14, 3–30.

Cheloni, D., Akinci, A. (2020). Source modelling and strong ground motion simulations for the 24 January 2020, *M*w 6.8 Elazığ earthquake, Turkey. *Geophys. J. Int.*, 223, 1054–1068.

Çoban, K.H., Sayıl, N. (2020). Different probabilistic models for earthquake occurrences along the North and East Anatolian fault zones. *Arabian Journal of Geosciences*, 13, 971.

Çınar, H., Alkan, H. (2017). Crustal S-wave structure around the Lake Van region (eastern Turkey) from interstation Rayleigh wave phase velocity analyses. *Turkish J Earth Sci.*,26, 73-90.

Çırmık, A. (2018). Examining the crustal structures of Eastern Anatolia, using thermal gradient, heat flow, radiogenic heat production and seismic velocities (Vp and Vs) derived from Curie point depth. *Bollettino di Geofi sica Teorica ed Applicata*, 59(2), 117–134.

Delph, J.R., Zandt, G., Beck, S.L. (2015). A new approach to obtaining a 3D shear wave velocity model of the crust and upper mantle: an application to eastern Turkey. *Tectonophysics*, 665, 92–100.

Desphande, A.A., Mohan, G. (2016). Seismic evidence of crustal heterogeneity beneath the Northwestern Deccan volcanic province of India from joint inversion of Rayleigh wave dispersion measurements and P receiver functions. *Journal of Asian Earth Sciences*, 128, 54–63.

Dewey, J.F., Hempton, M.R., Kidd, W.S.F., Saroglu, F., Sengor, A.M.C. (1986). Shortening of continental lithosphere: The neo-tectonics of eastern Anatolia-a young collision zone. *In M. P. Coward and A. C. Reis (Eds.), Collision tectonics*, (3–36). London: Geological Society.

Dziewonski, A., Bloch, S., Landisman, M. (1969). A technique for the analysis of transient seismic signals. *Bull. Seismol. Soc. Am*., 1, 427–444.

Gilligan, A., Roecker, S.W., Priestley, K.F., Nunn, C. (2014). Shear velocity model for the Kyrgyz Tien Shan from joint inversion of receiver function and surface wave data. *Geophys. J. Int.*, 199, 480–498.

Goforth, T., Herrin, E. (1979). Phase-matched filters: application to study of Love waves. *Bull. Seismol. Soc. Am*., 69, 27–44.

Gonzalez, O.L., Moreno, B., Romanelli, F., Panza, G.F. (2012). Lithospheric structure below seismic stations in Cuba from the joint inversion of Rayleigh surface waves dispersion and receiver functions. *Geophys. Journal Int.*, 1-13.

Gökalp, H. (2012). Tomographic imaging of the seismic structure beneath the East Anatolian Plateau. *Eastern Turkey Pure Appl Geophys*., 169, 1749-1776.

Helffrich, G., Wookey, J., Bastow, I. (2013). The Seismic Analysis Code, A Primer and User's Guide. Cambridge. United Kingdom.

Herrmann, R.B., Ammon, C.J. (2002). Computer program in seismology: surface waves, receiver functions and crustal structure. *In: S.L. University (Editor).*

Herrmann, R.B. (2013). Computer programs in seismology: an evolving tool for instruction and research. *Seismol. Res. Lett*., 84, 1081–1088.

Jamalreyhani, M., Büyükakpınar, P., Cesca, S., Dahm, T., Sudhaus, H., Rezapour, M., Isken, M.P., Asayesh, B.M., Heimann, S. (2020). Seismicity related to the eastern sector of Anatolian escape tectonic: the example of the 24 January 2020 Mw 6.77 Elazığ-Sivrice earthquake. *Solid Earth*, https://doi.org/10.5194/se-2020-55.

Julia, J., Ammon, C.J., Herrmann, R.B., Correig, A.M. (2000). Joint inversion of receiver function and surface wave dispersion observations. *Geophys. J. Int.*, 143, 99–112.

Kennett, B.L.N., Engdahl, E.R., Buland, R. (1995). Constraints on seismic velocities in the Earth from traveltimes, *Geophys. J. Int*., 122, 108–124.

Kind, R., Eken, T., Tilmann, F., Sodoudi, F., Taymaz, T., Bulut, F., et al. (2015). Thickness of the lithosphere beneath Turkey and surroundings from S-receiver functions. *Solid Earth*, 6, 971–984.

Langston, C.A. (1977). Corvallis, oregon, crustal and upper mantle receiver structure from teleseismic P and S waves. *Bullet. Seismol. Soc. Am.*, 67(3), 713–724.

Ligorria, J.P., Ammon, C.J. (1999). Iterative deconvolution and receiver function estimation. *Bullet. Seismol. Soc. Am*., 89(5), 1395–1400.

Lü, Y.S., Ni, L., Chen, Q.F. (2017). Pn tomography with Moho depth correction from eastern Europe to western China. *J Geophys Res. Solid Earth*, 122, 1284–1301.

Mahatsente, R., Önal, G., Çemen, I. (2018). Lithospheric structure and the isostatic state of Eastern Anatolia: Insight from gravity data modelling. *Lithosphere*, 10(2), 279–290.

McClusky, S., Balassanian, S., Barka, A., Demir, C., Ergintav, Georgiev, I., et al. (2000). Global Positioning System constraints on plate kinematics and dynamics in the eastern Mediterranean and Caucasus. *Journal of Geophysical Research*, 105, 5695–5719.

Melgar, D., Ganas, A., Taymaz, T., Valkaniotis, S., Crowell, B.W., Kapetanidis, V., Tsironi,V., Yolsal-Çevikbilen, S., Öcalan, T. (2020). Rupture kinematics of 2020 January 24 *M*w 6.7 Doğanyol-Sivrice, Turkey earthquake on the East Anatolian Fault Zone imaged by space geodesy. *Geophys. J. Int.*, 223, 862–874.

Motavalli-Anbaran, S.H., Zeyen, H., Jamasb, A. (2016). 3D crustal and lithospheric model of the Arabia–Eurasia collision zone. *J. Asian Earth Sci*., 122, 158–167.

Oruç, B., Gomez-Ortiz, D., Petit, C. (2017). Lithospheric flexural strength and effective elastic thicknesses of the Eastern Anatolia (Turkey) and surrounding region. *J Asian Earth Sci*., 150, 1–13.

Ozer, C., Ozyaziciglu, M., Gök, E., Polat O. (2019). Imaging the Crustal Structure Throughout the East Anatolian Fault Zone, Turkey, by Local Earthquake Tomography. *Pure Appl. Geophys*., 176, 2235–2261.

Özacar, A.A., Zandt, G., Gilbert, H., Beck, S.L. (2010). Seismic images of crustal variations beneath the East Anatolian Plateau (Turkey) from teleseismic receiver functions. *Geology Society London Special Publications*, 340, 485–496.

Öztürk, S., Bayrak Y. 2012. Spatial variations of precursory seismic quiescence observed in recent years in the Eastern part of Turkey. *Acta Geophysica*, 60(1), 92-118.

Öztürk, S. (2017). Space-time assessing of the earthquake potential in recent years in the Eastern Anatolia region of Turkey. *Earth Sciences Research Journal*, 21 (2), 67-75.

Öztürk, S. (2018). Earthquake hazard potential in the Eastern Anatolian Region of Turkey: seismotectonic b and Dc-values and precursory quiescence Z-value. *Front. Earth Sci*., 12(1), 215–236.

Pasyanos, M.E., Masters, T.G., Laske, G., Ma, Z. (2014). LITHO1.0: An updated crust and lithospheric model of the Earth. J. *Geophys. Res. Solid Earth*, 119, 2155-2173.

Reilinger, R., McClusky, S., Vernant, P., Lawrence, S., Ergintav, S., Cakmak, R., et al. (2006). GPS constraints on continental deformation in the Africa-Arabia-Eurasia continental collision zone and implications for the dynamics of plate interactions. *Journal of Geophysical Research, Solid Earth*, 111(B5), B05411.

Salah, M.K., Şahin, Ş. (2019). 3D crustal velocity and Vp/Vs structures beneath Southeast Anatolia and their geodynamic implications. *Геофизический журнал*, 2, 41.

Şengör, A.M.C., Yılmaz, Y. (1981). Tethyan evolution of Turkey: a plate tectonic approach. *Tectonophysics*, 75, 181–241.

Şengör, A.M.C., Görür, N., Şaroğlu, F. (1985). Strikeslip faulting and related basin formation in zones of tectonic escape Turkey as a case study. In: Biddle, K.T., Christie-Blick, K. (Eds.), Strike-slip Deformation Basin Formation and Sedimentation. *Soc. Econ. Paleontol. Miner. Spec. Publ*., 37, 227–264.

Tezel, T., Shibutani, T., Kaypak, B. (2013). Crustal thickness of Turkey determined by receiver function. *Journal of Asian Earth Sciences*, 75, 36–45.

Türkoğlu, E., Unsworth, M., Bulut, F., Çağlar, I. (2015). Crustal structure of the North Anatolian and East Anatolian Fault Systems from magnetotelluric data. *Physics of the Earth and Planetary Interiors*, 241, 1–14.

Wessel, P., Smith, W.H.F., Scharroo, R., Luis, J.F., Wobbe, F. (2013). Generic Mapping Tools: improved version released. *EOS Trans AGU*, 94:409–410.

Yön, B., Onat, O., Öncü, M.E., Karaşin, A. (2020). Failures of masonry dwelling triggered by East Anatolian Fault earthquakes in Turkey. *Soil Dynamics and Earthquake Engineering*, 133, 106-126.

Vanacore, E. A., Taymaz, T., Saygin, E. (2013). Moho structure of the Anatolian plate from receiver function analysis. *Geophysical Journal International*, 193(1), 329–337.

Vinnik, L. (1977). Detection of waves converted from P to SV in the mantle. *Physics of the Earth and Planetary Interiors*, 15, 39–45.

Warren, L.M., Beck, S.L., Biryol, C.B., Zandt, G., Ozacar, A.A., Yang, Y. (2013). Crustal velocity structure of Central and Eastern Turkey from ambient noise tomography. *Geophysical Journal International*. 194(3), 1941–1954.

Zor, E., Sandvol, E., Gurbuz, C., Turkelli, N., Seber, D., Barazangi, M. (2003). The crustal structure of the East Anatolian plateau (Turkey) from receiver functions. *Geophysical Research Letters*, 30(24), 8044.